On-chip optical trapping of extracellular vesicles using box-shaped composite SiO_2-Si_3N_4 waveguides

Loozen, Gyllion Brian; Caro, Jaap

DOI
10.1364/OE.26.026985

Publication date
2018

Document Version
Final published version

Published in
Optics Express

Research Article | Vol. 26, No. 21 | 15 Oct 2018 | OPTICS EXPRESS 26985
Optics EXPRESS

On-chip optical trapping of extracellular vesicles using box-shaped composite SiO_2-Si_3N_4 waveguides

GYLLION BRIAN LOOZEN* AND JACOB CARO

Department of Imaging Physics, Delft University of Technology, Lorentzweg 1, CJ Delft 2628, The Netherlands
**g.b.loozen@tudelft.nl*

Abstract: The application of on-chip optical trapping and Raman spectroscopy using a dual-waveguide trap has so far been limited to relatively big synthetic and biological particles (e.g., polystyrene beads and blood cells). Here, from simulations, we present the capabilities of dual-waveguide traps built from composite SiO_2-Si_3N_4 waveguides for optical trapping of extracellular vesicles (EVs). EVs, tiny cell-derived particles of size in the range 30–1000 nm, strongly attract attention as potential biomarkers for cancer. EVs are hard to trap, because of their smallness and low index contract w.r.t. water. This poses a challenge for on-chip trapping. From finite-difference time-domain simulations we obtain the narrow beam emitted from the waveguide facet into water, for $\lambda = 785$ nm. For a pair of such beams, in a counter-propagating geometry and for facet separations of 5, 10 and 15 μm, we derive the inter-facet optical field, which has a characteristic interference pattern with hot spots for trapping, and calculate the optical force exerted on EVs of size in the range 50–1000 nm, as a function of EV position. We use two refractive index models for the EV optical properties. Integration of the force curves leads to the trapping potentials, which are well-shaped in the transverse and oscillatory in the longitudinal direction. By applying Ashkin's criterion, the conditions for stable trapping are established, the central result of this work. Very small EVs can be stably trapped with the traps by applying a power also suitable for Raman spectroscopy, down to a smallest EV diameter of 115 nm. We thus argue that this dual-waveguide trap is a promising lab-on-a-chip device with clinical relevance for diagnosis of cancer.

OCIS codes: (140.7010) Laser trapping; (130.3120) Integrated optics devices; (170.4520) Optical confinement and manipulation; (230.7370) Waveguides; (180.5655) Raman microscopy.

References and links

1. G. Luka, A. Ahmadi, H. Najjaran, E. Alocilja, M. DeRosa, K. Wolthers, A. Malki, H. Aziz, A. Althani, and M. Hoorfar, "Microfluidics integrated biosensors: a leading technology towards lab-on-a-chip and sensing applications," Sensors (Basel) **15**(12), 30011–30031 (2015).
2. J. W. Chan, "Recent advances in laser tweezers Raman spectroscopy (LTRS) for label-free analysis of single cells," J. Biophotonics **6**(1), 36–48 (2013).
3. P. R. T. Jess, V. Garcés-Chávez, D. Smith, M. Mazilu, L. Paterson, A. Riches, C. S. Herrington, W. Sibbett, and K. Dholakia, "Dual beam fibre trap for Raman micro-spectroscopy of single cells," Opt. Express **14**(12), 5779–5791 (2006).
4. S. Dochow, M. Becker, R. Spittel, C. Beleites, S. Stanca, I. Latka, K. Schuster, J. Kobelke, S. Unger, T. Henkel, G. Mayer, J. Albert, M. Rothhardt, C. Krafft, and J. Popp, "Raman-on-chip device and detection fibres with fibre Bragg grating for analysis of solutions and particles," Lab Chip **13**(6), 1109–1113 (2013).
5. N. Bellini, K. C. Vishnubhatla, F. Bragheri, L. Ferrara, P. Minzioni, R. Ramponi, I. Cristiani, and R. Osellame, "Femtosecond laser fabricated monolithic chip for optical trapping and stretching of single cells," Opt. Express **18**(5), 4679–4688 (2010).
6. F. Bragheri, L. Ferrara, N. Bellini, K. C. Vishnubhatla, P. Minzioni, R. Ramponi, R. Osellame, and I. Cristiani, "Optofluidic chip for single cell trapping and stretching fabricated by a femtosecond laser," J. Biophotonics **3**(4), 234–243 (2010).
7. O. G. Hellesø, P. Løvhaugen, A. Z. Subramanian, J. S. Wilkinson, and B. S. Ahluwalia, "Surface transport and stable trapping of particles and cells by an optical waveguide loop," Lab Chip **12**(18), 3436–3440 (2012).

#335558 https://doi.org/10.1364/OE.26.026985
Journal © 2018 Received 27 Jun 2018; revised 31 Jul 2018; accepted 1 Aug 2018; published 2 Oct 2018

Optics EXPRESS

8. P. Løvhaugen, B. S. Ahluwalia, T. R. Huser, and O. G. Hellesø, "Serial Raman spectroscopy of particles trapped on a waveguide," Opt. Express **21**(3), 2964–2970 (2013).
9. M. Boerkamp, T. van Leest, J. Heldens, A. Leinse, M. Hoekman, R. Heideman, and J. Caro, "On-chip optical trapping and Raman spectroscopy using a TripleX dual-waveguide trap," Opt. Express **22**(25), 30528–30537 (2014).
10. I. Tatischeff, E. Larquet, J. M. Falcón-Pérez, P. Y. Turpin, and S. G. Kruglik, "Fast characterisation of cell-derived extracellular vesicles by nanoparticles tracking analysis, cryo-electron microscopy, and Raman tweezers microspectroscopy," J. Extracell. Vesicles **1**(1), 19179 (2012).
11. R. P. Carney, S. Hazari, M. Colquhoun, D. Tran, B. Hwang, M. S. Mulligan, J. D. Bryers, E. Girda, G. S. Leiserowitz, Z. J. Smith, and K. S. Lam, "Multispectral optical tweezers for biochemical fingerprinting of CD9-positive exosome subpopulations," Anal. Chem. **89**(10), 5357–5363 (2017).
12. Z. J. Smith, C. Lee, T. Rojalin, R. P. Carney, S. Hazari, A. Knudson, K. Lam, H. Saari, E. L. Ibañez, T. Viitala, T. Laaksonen, M. Yliperttula, and S. Wachsmann-Hogiu, "Single exosome study reveals subpopulations distributed among cell lines with variability related to membrane content," J. Extracell. Vesicles **4**(1), 28533 (2015).
13. F. Properzi, M. Logozzi, and S. Fais, "Exosomes: the future of biomarkers in medicine," Biomarkers Med. **7**(5), 769–778 (2013).
14. J. Skog, T. Würdinger, S. van Rijn, D. H. Meijer, L. Gainche, M. Sena-Esteves, W. T. Curry, Jr., B. S. Carter, A. M. Krichevsky, and X. O. Breakefield, "Glioblastoma microvesicles transport RNA and proteins that promote tumour growth and provide diagnostic biomarkers," Nat. Cell Biol. **10**(12), 1470–1476 (2008).
15. W. J. Allard, J. Matera, M. C. Miller, M. Repollet, M. C. Connelly, C. Rao, A. G. Tibbe, J. W. Uhr, and L. W. Terstappen, "Tumor cells circulate in the peripheral blood of all major carcinomas but not in healthy subjects or patients with nonmalignant diseases," Clin. Cancer Res. **10**(20), 6897–6904 (2004).
16. S. A. Melo, L. B. Luecke, C. Kahlert, A. F. Fernandez, S. T. Gammon, J. Kaye, V. S. LeBleu, E. A. Mittendorf, J. Weitz, N. Rahbari, C. Reissfelder, C. Pilarsky, M. F. Fraga, D. Piwnica-Worms, and R. Kalluri, "Glypican-1 identifies cancer exosomes and detects early pancreatic cancer," Nature **523**(7559), 177–182 (2015).
17. W. Lee, Optical Sciences, University of Twente, Drienerloolaan 5, Enschede 7500 AE, The Netherlands, A. Nanou, L.G. Rikkert, F.A.W. Coumans, C. Otto, L.W.M.M. Terstappen and H.L. Offerhaus are preparing a manuscript to be called "Label-free prostate cancer detection by characterization of extracellular vesicles using Raman spectroscopy."
18. S. Vyawahare, A. D. Griffiths, and C. A. Merten, "Miniaturization and parallelization of biological and chemical assays in microfluidic devices," Chem. Biol. **17**(10), 1052–1065 (2010).
19. A. Ashkin, J. M. Dziedzic, J. E. Bjorkholm, and S. Chu, "Observation of a single-beam gradient force optical trap for dielectric particles," Opt. Lett. **11**(5), 288–290 (1986).
20. TriPleX is a trademark for the waveguide technology of LioniX International BV.
21. K. Wörhoff, R. G. Heideman, A. Leinse, and M. Hoekman, "TriPleX: a versatile dielectric photonic platform," Adv. Opt. Technol. **4**(2), 189–207 (2015).
22. E. van der Pol, A. N. Böing, P. Harrison, A. Sturk, and R. Nieuwland, "Classification, functions, and clinical relevance of extracellular vesicles," Pharmacol. Rev. **64**(3), 676–705 (2012).
23. W. Choi, C. Fang-Yen, K. Badizadegan, S. Oh, N. Lue, R. R. Dasari, and M. S. Feld, "Tomographic phase microscopy," Nat. Methods **4**(9), 717–719 (2007).
24. H. J. van Manen, P. Verkuijlen, P. Wittendorp, V. Subramaniam, T. K. van den Berg, D. Roos, and C. Otto, "Refractive index sensing of green fluorescent proteins in living cells using fluorescence lifetime imaging microscopy," Biophys. J. **94**(8), L67–L69 (2008).
25. Lumerical FDTD Solutions, Inc., *http://www.lumerical.com/tcad-products/fdtd/* (accessed June 26, 2018).
26. The expression for the gradient force goes back to Eq. (2) of [16], the pioneering work of A. Ashkin. The difference with Eq. (2) in [16] involves typographic errors and our prefactor π instead of (1/2). Further, our equation has no minus sign and gives the direction of the force vector. Finally, we use SI units.
27. P. Zemánek, A. Jonaš, L. Šrámek, and M. Liška, "Optical trapping of Rayleigh particles using a Gaussian standing wave," Opt. Commun. **151**(4–6), 273–285 (1998).
28. M. Y. Wu, D. X. Ling, L. Ling, W. Li, and Y. Q. Li, "Stable optical trapping and sensitive characterization of nanostructures using standing-wave Raman tweezers," Sci. Rep. **7**(18042), 42930 (2017).
29. M. M. van Leest, F. Bernal Arango, and J. Caro, "Optical forces and trapping potentials of a dual-waveguide trap based on multimode solid-core waveguides," J. Eur. Opt. Soc. **6**, 11022 (2011).
30. J. Ježek, P. Zemánek, A. Jonáš, M. Šery, P. Pokorny, and M. Liška, "Behavior of nanoparticle and microparticle in the standing wave trap," Proc. SPIE **4356**, 318–326 (2001).
31. P. M. Bendix and L. B. Oddershede, "Expanding the optical trapping range of lipid vesicles to the nanoscale," Nano Lett. **11**(12), 5431–5437 (2011).
32. F. Schreuder, LioniX International BV, Hengelosestraat 500, 7521 AN Enschede, The Netherlands (personal communication, 2018).
33. A. Nanou, F. A. W. Coumans, G. van Dalum, L. L. Zeune, D. Dolling, W. Onstenk, M. Crespo, M. S. Fontes, P. Rescigno, G. Fowler, P. Flohr, C. Brune, S. Sleijfer, J. S. de Bono, and L. W. M. M. Terstappen, "Circulating tumor cells, tumor-derived extracellular vesicles and plasma cytokeratins in castration-resistant prostate cancer patients," Oncotarget **9**(27), 19283–19293 (2018).

Optics EXPRESS

1. Introduction

A class of lab-on-a-chip devices for optical analysis of particles is based on using integrated photonic waveguides for manipulating and spectroscopic fingerprinting the particles, with the goal of their identification. Possible application fields are various, and include point-of-care diagnostics and drinking water technology [1], with a focus on, for example, detection of human cells indicative of a disease and harmful bacteria. Examples in this field are labs-on-a-chip for optical trapping and Raman spectroscopy. These are on-chip versions of a laser-tweezers Raman spectroscopy (LTRS) setup [2]. LTRS unifies particle trapping with a focused laser beam and Raman spectroscopy of the trapped particle using the same concentrated light. This leads to Raman identification of the trapped particle. Prominent examples of on-chip versions are dual-fibre or dual-waveguide traps, often combined with microfluidics for particle supply. These traps are based on two opposing fibres or integrated photonics waveguides, from which counter-propagating beams emanate that define the concentrated optical field for trapping and Raman spectroscopy.

The dual-fibre trap in [3] has been used to hold and manoeuvre human cells to record their Raman signals. The trap in [4], apart from fibres for trapping and Raman generation, has fibers for collecting Raman signals. A preference is arising towards dual-*waveguide* devices based on *microfabricated* waveguides, thus avoiding delicate mounting of fibres and aiming for mass production. An important step in this direction is reported in [5,6], where the waveguides are created by local modification of the index of glass using accurate writing with a femtosecond laser beam. The resulting devices can successfully trap and stretch red blood cells (RBCs). The laser-writing technique is inherently sequential, making it particularly suitable for fast prototyping. We further mention the traps reported in [7,8], based on microfabricated Ta_2O_5 waveguides. In [7] trapping of synthetic particles and RBCs is demonstrated, with supply of particles to the trap by optical propulsion on the waveguides. In [8] Raman spectra of trapped synthetic spheres are reported, but the spectra are induced using a separate laser beam and not by the beams emitted by the waveguides. In our work [9], we have exploited the counter-propagating beams in a dual-waveguide trap built from special waveguides microfabricated with semiconductor processing techniques to their full capability, using the beams both for trapping synthetic particles and for inducing Raman signals from the trapped particles.

Recently, LTRS has been applied for studying human extracellular vesicles (EVs) [10–12]. These cell-derived particles are present in bodily fluids such as urine and have a diameter ranging from 30 to 1000 nm, the size-distribution's maximum occurring below 200 nm. An EV comprises a lipid-bilayer membrane of the parental cell, enclosing mainly cell-derived cytoplasm with suspended DNA, RNA and proteins. Tumor-derived EVs strongly attract attention as potential biomarkers for cancer [13,14]. For cancer diagnosis such EVs may play a role similar to that of circulating tumor cells (CTCs [15],). The bio-chemical composition of a fraction of EVs may already deviate from regular in a very early stage of carcinogenesis of the organ from which the EVs derive [16], while presence of CTCs indicates full existence of organ cancer. Thus, determining EV composition using LTRS can lead to early cancer diagnosis [17]. However, only a small sub-population of EVs in bodily fluids shows a signature of carcinogenesis, if present. This circumstance asks for high throughput platforms, *e.g.* lab-on-a-chip devices scaled to versions with multiple parallelism [18]. Further, EVs are very small and have a low index contrast w.r.t. the suspending medium, making on-chip optical trapping of EVs challenging.

Here, from a simulation study, we present the capabilities for trapping of EVs of the dual-waveguide trap we apply in [9]. The novelty compared to [9] is that we here simulate for this type of trap the full range of optical and trapping properties, leading to qualification for the characterization of EVs. Further, our simulation results provide guidance for design and development of dual-waveguide devices for optical trapping and Raman spectroscopy of a broad range of bio-particles relevant for health and medicine.

Optics EXPRESS

First, the device geometry and two index models for EVs are presented, followed by a description of the simulation approach. Then, we detail the photonic ingredients of the traps, *viz.* the waveguide mode, the emitted on-chip beam and the energy density in the trap. Subsequently, the force curves for three trap sizes and the index models yield the trapping potentials. These in turn, via Ashkin's criterion [19], lead to the conditions for stable EV trapping, which constitute the central results of this work. It follows that very small EVs can be trapped with the dual-waveguide traps, highlighting the clinical relevance of this lab-on-a-chip as a basic device for high throughput platforms.

2. Device geometry and optical models for EVs

The building block of the dual-waveguide trap is a waveguide with a box-shaped composite Si_3N_4–SiO_2 structure. Its cross section of 1 × 1 μm^2 is shown in Fig. 1(a). The walls of the square box are 50 nm thick Si_3N_4 layers. The material inside and outside the box is SiO_2. With this structure we model the slightly trapezoidal TripleX [20,21] waveguides we apply for the dual-waveguide trap in [9].

The geometry of the dual-waveguide trap built from a pair of such waveguides is depicted in Fig. 1(b). The waveguides are opposed and guide light to a fluidic channel, used for supply of EVs. The waveguide facets, which emit a narrow light beam, are part of the walls of the fluidic channel. The counter-propagating beams created in this way define a strongly confined optical field and thus form an optical trap. The gap width *w* between the waveguide facets is 5, 10 or 15 μm, equal to the widths in the devices leading to the results in [9]. The trap centre is the origin of the coordinate-system (see Fig. 1(b)). The *x*-direction is the longitudinal direction and the *y*- and *z*-directions are the transverse directions.

EVs are spherical particles [22], with a diameter d_{EV}. We represent their optical properties by two models for the refractive index n. The first model assumes a homogeneous EV index, for which we take $n_{hom} = 1.37$ [23]. In the second model we apply the realistic core-shell structure of EVs, using $n_{core} = 1.37$ and $n_{shell} = 1.46$ [24], and taking a shell thickness of 5 nm. The homogeneous index can be accurate enough for big vesicles since these have a small surface-to-volume ratio. The core-shell model will be more appropriate for small vesicles since for these the shell contribution to the total optical force is expected to be rather high.

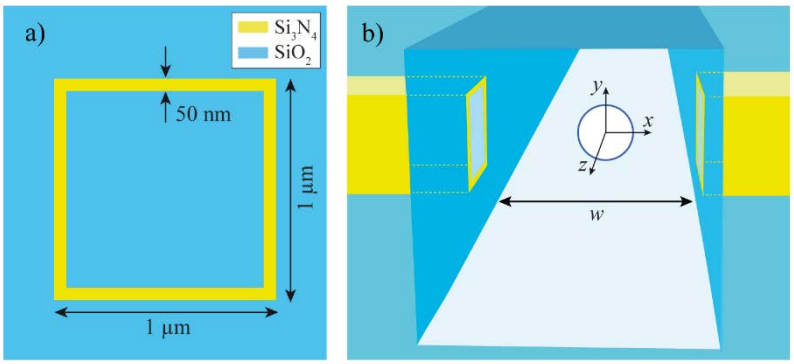

Fig. 1. (a) Cross section of the composite SiO_2–Si_3N_4 waveguide, the building block of the dual-waveguide trap. The material inside and outside the square box with Si_3N_4 walls is SiO_2. (b) Three-dimensional impression of the dual-waveguide trap. The waveguide facets, with separation *w*, are part of the walls of the fluidic channel. The origin of the coordinate system is the trap centre, where in the figure an EV is located with a core-shell structure.

Optics EXPRESS

3. Simulation approach

We derive the electromagnetic fields in the traps with the 3D finite-difference time-domain (FDTD) method, using Lumerical FDTD solutions [25]. The first goal is to obtain the optical forces acting on an EV, as a function of its position on the three axes defined in Fig. 1(a), and for the 10 or 15 μm traps on other axes parallel to the *y*-axis. This is done by simulating traps containing an EV and empty traps. The fields with the EV in the trap are needed for Lumerical's force calculations. The fields for the empty trap are used to independently calculate the forces for comparison with Lumerical's method, as discussed below.

The TE mode obtained from Lumerical's mode solver is excited in each waveguide, for wavelength $\lambda_0 = 785$ nm . This is our preferential wavelength [9], in view of generating Raman signals from the trapped particle. We use planar sources, placed at 2 μm from the waveguide facet, that oscillate in phase and emit a short Gaussian pulse of carrier frequency $f = c/\lambda_0$, the frequency corresponding to the mode's wavelength. The time traces of the electromagnetic fields at each mesh point are Fourier transformed to obtain the spatial dependence of the complex amplitudes of the harmonic fields for λ_0 . This procedure yields the beams emitted from the facets, which according to the TE polarization have $\vec{E} // \hat{z}$.

The mesh size must be small enough to resolve the fields, on the scale of i) the wavelength in the highest index material, ii) the smallest structure of the device and iii) the details of the EV structure. The simulation time, however, is inversely proportional to the mesh size to the fourth power, implying a practical limit. To fulfill the mesh-size requirements, while keeping simulation time within reasonable bounds, we subdivide the total simulation domain into three subdomains of different mesh size. The total simulation domain is 17 and 11 μm in the *y*- and *z*-direction, respectively. The length in the *y*-direction exceeds that in the *x*-direction for the TE polarization used, in view of the side lobes emitted away from the beam axis (see Section 4). In the *x*-direction the simulation domain is $w + 5.4$ μm. At the domain's boundaries we use 2 μm thick perfectly matched absorbing layers.

The first subdomain is a rectangular block of cross section 2 × 2 μm^2, enclosing the waveguides. It has mesh size $\Delta_1 = 10$ nm , imposed by the Si_3N_4 waveguide walls. The block length equals the total domain's length in the *x*-direction. The second subdomain is a cube of edge $d_{EV} + 10\Delta_2$ surrounding the EV. For the homogeneous index model, we choose $\Delta_2 = d_{EV}/20$, with an upper limit of 10 nm. For the core-shell model we take $\Delta_2 = 2$ nm , in view of the thin EV shell. The third subdomain is the remainder of the total domain, for which we take $\Delta_3 = \lambda_0/(14 n_{SiO2})$. In simulating the empty trap, we use $\Delta_4 = 10$ nm in the first and second subdomain and $\Delta_3 = \lambda_0/(14 n_{SiO2})$ in the third subdomain.

We obtain the time-averaged force $< \vec{F} >$ acting on an EV using Lumerical's volumetric technique, by calculating the volume integral of the time-averaged Lorentz force density for a cube enclosing the EV. The edge of the integration cube is $d_{EV} + 7\Delta_2$, some smaller than the cube's edge that defines the sub-meshing. The Lorentz force density $< \vec{f} >$ is calculated at each mesh point inside the cube and on its faces using:

$$< \vec{f} >= \varepsilon_0 \varepsilon_b \left(\vec{\nabla} \cdot < \vec{E} > \right) < \vec{E} > + i\omega \varepsilon_0 (\varepsilon_{EV} - \varepsilon_b) < \vec{E} > \times < \vec{B} > . \qquad (1)$$

Here $< \vec{E} >$ and $< \vec{B} >$ are the position dependent time-averaged electric and magnetic field, respectively, with the EV in the trap. ε_0 is the vacuum permittivity, while ε_b and ε_{EV} are the relative permittivity of the background medium (*i.e.* water) and the EV, respectively, the latter being a function of position for the core-shell model. We assume lossless materials, implying that the relative permittivities equal the square of the refractive indices. $\omega = 2\pi c / 785$ nm is

Optics EXPRESS

the angular frequency of the light. The force on the background medium in the integration cube does not contribute to the net force on the EV. Based on the symmetry of the device geometry, we limit the force calculations to the three half-axes of the first octant, which gives all relevant information on the force behavior in the complete three-dimensional system. For a simulation of a single force point, *i.e.* for a single EV position, we used five so-called thin nodes of a supercomputer, each having 24 cores operating at 2.4 or 2.6 GHz, and 64 GB of RAM. On average such a single point simulation takes 10 minutes.

To calculate the forces for the smaller EVs with an independent approach, enabling comparison with Lumerical's method applied to EVs with an assumed homogenous index, we use the expression for the so-called time-averaged gradient force acting on a homogeneous dielectric particle, here an EV [26]:

$$< \vec{F} > = \frac{\pi \varepsilon_0 \varepsilon_b d_{\mathrm{EV}}^3}{8} \left(\frac{m^2 - 1}{m^2 + 2} \right) < \vec{\nabla} \left| \vec{E} \right|^2 >, \quad m = \varepsilon_{\mathrm{EV}} / \varepsilon_{\mathrm{b}}. \tag{2}$$

Here <···> again denotes time-averaging, while in this case $\vec{E}$ is the electric field in the empty trap. Equation (2) is valid for a dielectric particle small enough for the electric field to be virtually constant throughout its volume. For such particles the gradient force accurately represents the full optical force of a trap provided the scattering force is negligible or zero. This situation is known to occur in and close to the centre of free space traps with counter-propagating beams of equal intensity [27,28].

The gradient force of Eq. (2) inherently is a conservative force. Consequently, in the approximation of negligible scattering force, a unique value of the trapping potential can be assigned at any point by integrating the force along a suitable path. We anticipate that the forces of the dual-waveguide trap obtained with the volumetric technique are rather close to the gradient force and thus can be considered as conservative. Therefore, we derive the position dependent optical potential by integrating the force obtained with the volumetric technique. For example, the transverse potential $U_y(x_0, y_0, 0)$ in the point y_0 for an axis parallel to the *y*-direction through the point $(x_0, z = 0)$ ($x_0, y_0 \geq 0$, the negative branches follow from symmetry) is given by:

$$U_y(x_0, y_0, 0) = -\int_{\infty}^{y_0} < F_{x_0, y, 0}(y) > \mathrm{d}y. \tag{3}$$

In Eq. (3) x_0 ($x_0 \geq 0$) is the position of the minimum of the global potential for the x direction (see Section 7). For the 5 µm trap a single minimum occurs at $x_0 = 0$. For the 10 and 15 µm traps, x_0 is the position of one of the minima of the (symmetric) double-well potential, which is located near the facet (see Section 7). Loosely, the potential given by Eq. (3) will further be called U_y. For U_z an equation similar to Eq. (3) holds. For the *x*-direction F_x is only defined between the waveguide facets. Therefore, to calculate the longitudinal potential $U_x(x_0)$ we limit the integration interval such that the EV is not in contact with the facet. This leads to:

$$U_x(x_0) \equiv U(x_0, 0, 0) = -\int_{x_1}^{x_0} < F_x(x) > \mathrm{d}x. \tag{4}$$

Here, we choose $x_1 = (w + d_{\mathrm{EV}})/2 - 3\Delta_2$. We add a constant to the outcome of Eq. (4), such that $U_x(0) = U_y(0)$.

Calculating the potential for three axes, yields the main information on the potential wells. For stable trapping of an EV the potential well should be deep enough. For this we use Ashkin's

Optics EXPRESS

stability criterion, according to which trapping in a potential well of depth U_0 is stable for $U_0 / kT \geq 10$ [19]. Since the well depth is proportional to the optical power supplied to the trap by the waveguides, the criterion leads to a condition for the optical power.

4. Waveguide mode, emitted beam, and energy density in the trap

We have calculated the TE mode of the waveguide of Fig. 1(a) using Lumerical's mode solver for $\lambda = 785$ nm. At this wavelength the waveguide supports a single mode per polarization. We use refractive indices of 2.00, 1.45 and 1.33 for Si_3N_4, SiO_2 and water, respectively. The mode profile is shown in Fig. 2(a), where the colors represent the intensity of the light. As can be seen, for this polarization the electric field concentrates in the upper and lower Si_3N_4 walls of the box. Further, the field is relatively low in the interior of the box (SiO_2), quite contrary to the case of usual homogeneous ridge waveguides. The electric field drops abruptly upon entering the vertical walls of the box from inside or outside, satisfying the boundary condition for the normal component for the dielectric displacement.

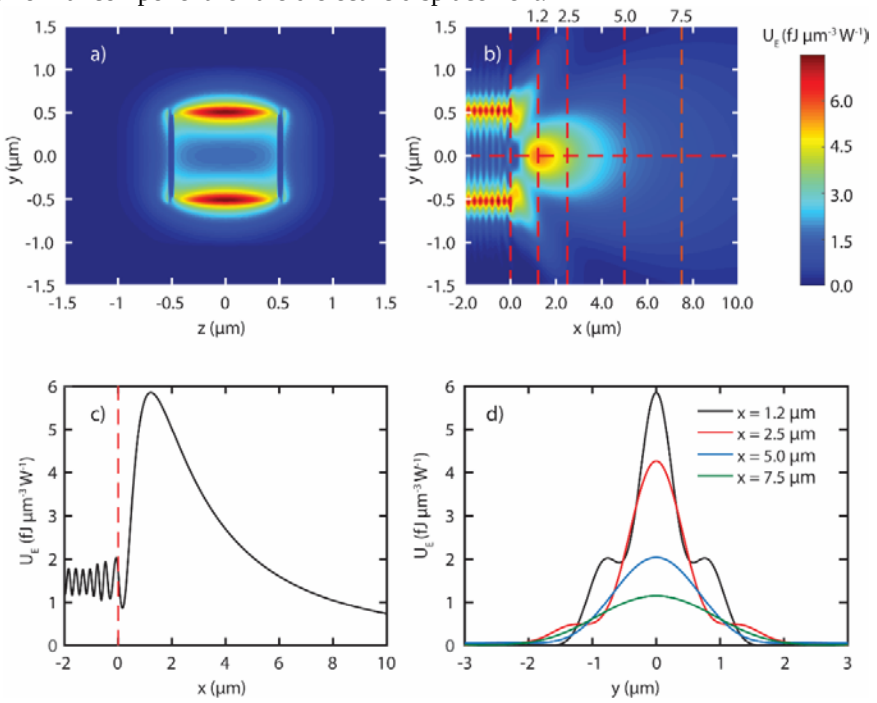

Fig. 2. (a) Profile of the TE mode of the waveguide in Fig. 1(a), for a wavelength of 785 nm. The colors indicate intensity, red (blue) meaning high (low), and do not relate to the scale bar to the right. (b) Energy density of the optical field in the *xy*-plane, both in the waveguide and the water, obtained from a FDTD simulation. The horizontal dashed line is the beam axis. Vertical dashed lines indicate the facet position and are the transverse lines for which in (d) beam profiles are plotted. The color bar defines the energy-density values. (c) Longitudinal energy-density profile on the beam axis. (d) Transverse beam profiles on the axes in (b).

FDTD simulation leads to the energy-density distribution in the xy-plane in Fig. 2(b), both in the waveguide and the water, using a source in the waveguide emitting 1 W of power towards the facet. At the facet the guided mode is converted into radiation modes that enter the water present for $x \geq 0$. The oscillatory pattern inside the waveguide and its walls represents a standing wave resulting from interference of the forward propagating mode and its part reflected back from the facet. Near the facet, the radiation modes take the form of two coherent beamlets emitted by the upper and lower waveguide walls. These beamlets merge, yielding a main beam (further called beam) coaxial with the waveguide axis, which co-exists with two

Optics EXPRESS

side lobes directed away from the axis. The beam reaches its energy-density maximum on the axis at 1.2 μm from the facet, whereafter it decays smoothly and simultaneously broadens. The maximum and the decay of the beam are quantified by the longitudinal energy-density profile plotted in Fig. 2(c). The transverse beam profiles in Fig. 2(d) further quantify the beam, in particular its spreading with increasing distance to the facet. The transverse profiles show shoulders at distances of 1.2 and 2.5 μm that arise from the aforementioned side lobes. We have compared the beam in Fig. 2(c) with the one we report in [29] for a Si_3N_4 solid core waveguide of the same cross section. We find that the decay length of the present beam is about three times longer and the beam spreading correspondingly weaker, meaning that the composite Si_3N_4–SiO_2 waveguide produces a tighter beam and thus is a better waveguide to build a strong optical trap.

For three traps built from the waveguide of Fig. 1(a) with facet separations of 5, 10 and 15 μm we have simulated the optical fields resulting from the coherent counter-propagating beams. In Fig. 3 we show time averaged energy-density distributions in *xy*-plane of the traps. A total power of 1W is supplied to the traps, each waveguides contributing 0.5 W. We omit the distribution in the *xz*-plane, since it portrays the same type of behavior.

A common characteristic of the traps is the interference pattern between the facets, which has a period of 306 nm. The EV size distribution is such that a small EV can be locally trapped at a single maximum of the interference pattern, here further called hot spot. But also multiple small EVs may be trapped at one hot spot, similar to trapping of multiple EVs with a laser trap [10]. A hot spot is narrower in the longitudinal than in a transverse direction. Therefore, the confined Brownian motion of an EV has wider excursions in a transverse than in the longitudinal direction.

The three traps, however, also show an important difference concerning the position of the regions where the interference maxima are strongest, *i.e.* the so-called global hot regions. For the 5 μm trap a single global hot region exists (see Fig. 3), symmetrically placed around

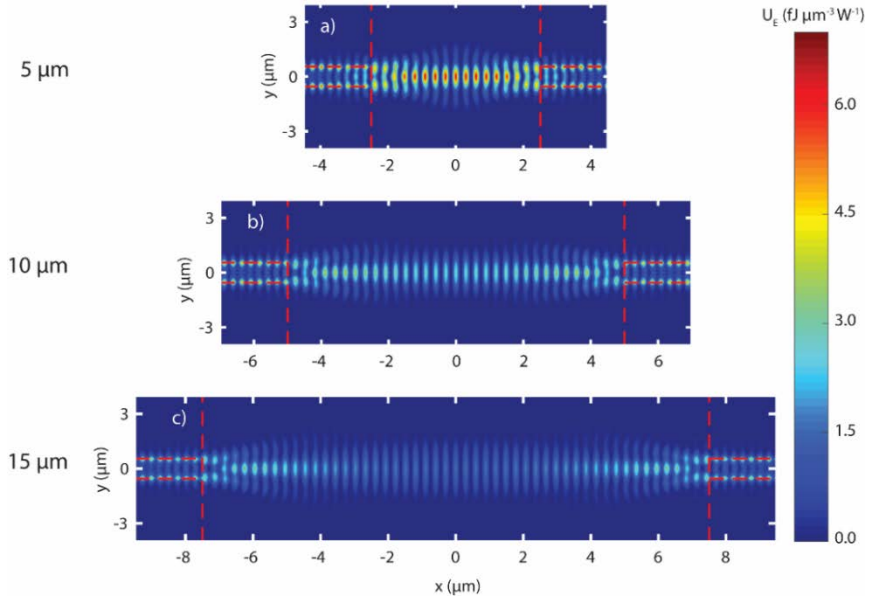

Fig. 3. Time averaged energy density in the *yx*-plane for dual-waveguide traps with a facet separation of 5, 10 and 15 μm. The total power supplied to each trap is 1 W. The 5 μm trap has one global hot region centred between the facets. The 10 and 15 μm traps have two global hot regions, each near a facets. The color bar defines the energy-density values.

the center. The 10 and 15 μm traps, on the contrary, have two global hot regions near the facets. This difference results from the longitudinal profile of the interfering beams shown in Fig. 2(c),

Optics EXPRESS

in particular their decay and the position of their maximum. These are such that the central global hot region of the 5 μm gap is split into two global hot regions for the wider gaps. We note that the trap built from Si_3N_4 solid core waveguides [29] already shows two global hot regions for facets 5 μm apart. This agrees with the weaker beam decay in the present traps.

5. Force characteristics of the traps

We have calculated the longitudinal force curve $F_x(x)$ and the transverse force curves $F_y(y)$ and $F_z(z)$ in the traps. For up to about two dozen diameters of homogeneous EVs in the range 50–1000 nm and for 6 diameters of core-shell EVs in the range 50–450 nm such curves have been obtained, of which a fraction is shown in Fig. 4. Forces acting on homogeneous EV have also been calculated using Eq. (2), giving the gradient force. Gradient-force data are included in Fig. 4(a), 4(b) and 4(c) for d_{EV} = 100 nm (black dots), but such data have been obtained for other diameters as well. We concentrate on the 5 and 15 μm traps, since qualitatively results for the 10 μm trap are very similar to those of the 15 μm trap.

In Figs. 4(a), 4(b) and 4(c) curves $F_y(y)$, $F_z(z)$, and $F_x(x)$ for the 5 μm trap are shown, respectively, for diameters as indicated and in Fig. 4(a) and 4(b) for both index models. The unit of force is pN/W, *i.e.* the force is normalized to the power delivered to the trap. In Fig. 4(d) $F_x(x)$ is shown for the 15 μm trap, restricted to homogeneous EVs of the same diameters as in the other sub-figures. In view of symmetry, the plots are limited to the positive half axes. Transverse force curves for the 15 μm trap are omitted, since qualitatively these are similar to those of the 5 μm trap in Fig. 4(a). In condensed form, the properties of the *three* traps are *quantitatively* reflected by trap stiffnesses in Table 1 below and by stability curves in Section 7.

$F_y(y)$ for the 5 μm trap is linear near the origin and has a negative slope. This reflects the restoring character of a Hookean force pulling back the EV to the hot spot at the origin, a behavior described by $F_y(y) = -\kappa_y y$, with κ_y the normalized stiffness for the *y*-direction. Normalized stiffnesses for the other directions are defined accordingly. With increasing distance $|F_y(y)|$ reaches an absolute maximum, followed by a local maximum. The absolute maximum relates to the maximum gradient of the beam in Fig. 2(b). The local maximum relates to the side lobes in that figure. For d_{EV} = 1000 nm, the local maximum is less pronounced, since the EV for this size overlaps with both the beam and the side lobe, making their individual contributions less distinct. This behavior of $F_y(y)$ applies to both index models, but for small diameters the force on core-shell EVs (curves shown for d_{EV} = 100, 150 nm) is considerably higher than that for homogeneous EVs. For d_{EV} = 50 nm, F_y on average is 110% higher for the core-shell EV than for the homogeneous EV, while for d_{EV} = 250 nm the percentage still is 25%. For d_{EV} = 500 nm the forces for the two models are virtually the same. Apparently, for the smaller diameters the shell, though only 5 nm thick, contributes significantly to the force and thus cannot be omitted in the EV model.

As can be seen in Fig. 4(b), $F_z(z)$ behaves very much the same as $F_y(y)$, the differences being that $|F_z(z)|$ is some smaller than $|F_y(y)|$, accompanied by a slightly less steep initial slope, that the maximum of $|F_z(z)|$ occurs at a slightly larger distance and that a local minimum of $|F_z(z)|$ is absent. These differences can be traced back to a less tight beam in the *xz*-plane and absence of side lobes in that plane. $F_y(y)$ and $F_z(z)$ being so close, we will further refer to $F_y(y)$ as the transverse force.

Optics EXPRESS

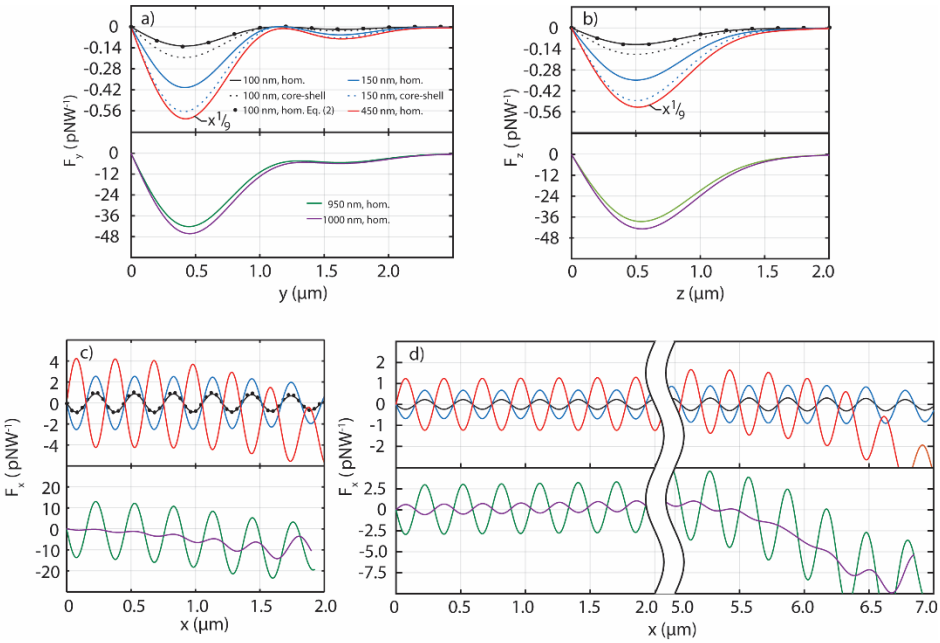

Fig. 4. Force curves for the 5 and 15 μm traps, calculated using the volumetric technique. The black dots have been obtained using Eq. (2). The legends in (a) define EV size and EV index model (homogeneous vs. core-shell) and apply to each panel. (a) Transverse force $F_y(y)$ for the 5 μm trap. (b) Transverse force $F_z(z)$ for the 5 μm trap. (c) Longitudinal force $F_x(x)$ for the 5 μm trap. (d) Longitudinal force $F_x(x)$ for the 15 μm trap, with part of the *x*-axis omitted to obtain the same horizontal scale as in (a-c). The curves in (a-d) are piecewise cubic spline interpolations between the data points. $F_y(y)$ and $F_z(z)$ curves have 15 data points. $F_x(x)$ curves have 33 data points per μm.

$F_x(x)$ is an oscillatory function, as exemplified in Figs. 4(b) and 4(c) for the 5 and 15 μm traps. The oscillation period equals the period of the fields in Fig. 3, implying that the origin is interference. As a function of EV size, a hot spot of the interference pattern attracts or repels the EV, depending on whether the local force-curve slope is negative or a positive. In Figs. 4(b) and 4(c) attraction occurs for 100, 150 and 950 nm, while repulsion occurs for 450 and 1000 nm. This sign reversal of the force agrees with [30], which reports that the sign in a standing wave trap depends periodically on particle size and that the particle's equilibrium position alternates between interference maxima and minima. Further [30], particle sizes exceeding the interference-pattern period exist for which the net optical force is zero as a result of complete cancellation of attractive forces of neighbouring hot spots. For the 1000 nm EV this cancellation almost occurs, giving weak oscillations in Figs. 4(b) and 4(c). EVs clearly smaller than the interference-pattern period are attracted by only a single hot spot, giving an amplitude of $F_x(x)$ considerably higher than the maximum of $|F_y(y)|$. This results from the spot's stronger intensity gradient in the *x*-direction than in the *y*-direction. This difference in force strength for the two directions can clearly be seen from the curves for 100 and 150 nm EVs in Figs. 4(a) and 4(c).

The global hot region of the 5 μm trap is centered at $x = 0$. Therefore, for the smaller EVs the force oscillations in Fig. 4(b) are weaker towards the facets. The hot spots near the origin thus are more preferential trapping sites, and one may expect the type of hopping motion we report in [9] towards the center of the global hot region. For the 1000 nm EV the situation is different, since for this size the less intense hot spots near the facet lead to increasingly weaker

Optics EXPRESS

cancellation near the facet. Preferential trapping is still at the origin, in view of the force direction imposed by the background, on which the oscillations are superimposed.

For the 15 μm trap the global hot regions are located near the facets. For most of the diameters in Fig. 4(c) this leads to stronger oscillations with increasing distance from the center and thus to stronger local traps near the facets. For the 1000 nm EV the changed position of the global hot region leads to weaker oscillations towards the facet, followed by a few strong oscillations as a result of entering the relatively "cold" on-axis region very close to the facet (see Fig. 3).

We now compare the forces obtained using the volumetric technique and the gradient formula Eq. (2). In Figs. 4(a) and 4(b) it is seen that the results for d_{EV} = 100 nm agree very well. The relative root-mean-square deviation between the forces according to the models amounts to 7% for $F_y(y)$ and 11% for $F_x(x)$. For d_{EV} = 50 nm (curve not shown) these differences are 2.9% and 2.5%, respectively. These differences indicate that the scattering force in this size range is only a small fraction of the total force. This results from the counter-propagation of the beams of low divergence. For larger EVs the difference increases, indicating break down of the dipole approximation, on which the gradient formula is based.

Table 1. Normalized trap stiffnesses κ_x and κ_y of the strongest trapping sites for the three traps for diameters of core-shell EVs as indicated. The quantities d_{EV}, *w*, $\kappa_{x(y)}$ denote EV diameter, facet separation of the trap, and stiffnesses for the *x*(*y*)-direction, respectively.

d_{EV} (nm)	*w*(μm)	κ_x (fN/nm/W)	κ_y (fN/nm/W)
50	5	5.12	0.13
	10	2.57	0.10
	15	1.81	0.09
100	5	28.63	0.80
	10	14.35	0.59
	15	10.11	0.59
150	5	72.07	2.21
	10	36.12	1.70
	15	25.41	1.71

In Table 1 the values of the normalized trap stiffnesses κ_x and κ_y for the traps are compiled for 50, 100 and 150 nm core-shell EVs and for the strongest trapping sites, *i.e.* for the most intense hot spots of the respective global hot regions. The forces for the *y*- and *z*-direction being very comparable, κ_y is taken as representative for κ_z. The Table shows that both κ_x and κ_y decrease with increasing facet separation. This arises from the decreasing maximum constructive interference of the beams. Further, all κ_x strongly exceed the related κ_y owing to the much stronger gradients in the *x*-direction. Finally, the systematic increase of κ_x and κ_y with EV size for each trap agrees with the diameter dependence of the power required to trap core-shell EVs (Section 7).

We compare the stiffnesses in Table 1 to those in [31], which reports trapping experiments on synthetic core-shell EVs using a focussed laser beam. For EV diameters in the range 50-150 nm lateral stifnesses in the range 1-7 fN/nm/W are reported [31]. Our κ_x values in Table 1 clearly exceed these laser-trap values, while our κ_y values are smaller. Since for a laser trap the axial stifness is several times smaller than its lateral stiffness, it follows that the important difference and advantage of the dual-waveguide trap for trapping of these nanometer-scale EVs is the up to ten times higher stiffness in the *x*-direction. This results from the interference of the beams.

Optics EXPRESS

6. Trapping potentials

We have integrated the force curves to obtain the trapping potentials, as prescribed in Section 3. From the forces in Fig. 4, a single potential well is expected for the transverse directions and a periodic potential for the longitudinal direction. Indeed, such behavior is seen in Fig. 5, which shows the potentials $U_y(y)/kT$ [at $(x,z)=(0,0)$] and $U_x(x)/kT$ [at $(y,z)=(0,0)$] derived from the force curves in Figs. 4(a), 4(c), and 4(d) for a power of 100 mW supplied to the trap, again using half axes. The potentials are normalized to kT (T = 293 K) to easily connect to the criterion for stable trapping $U_0/kT \geq 10$ [19].

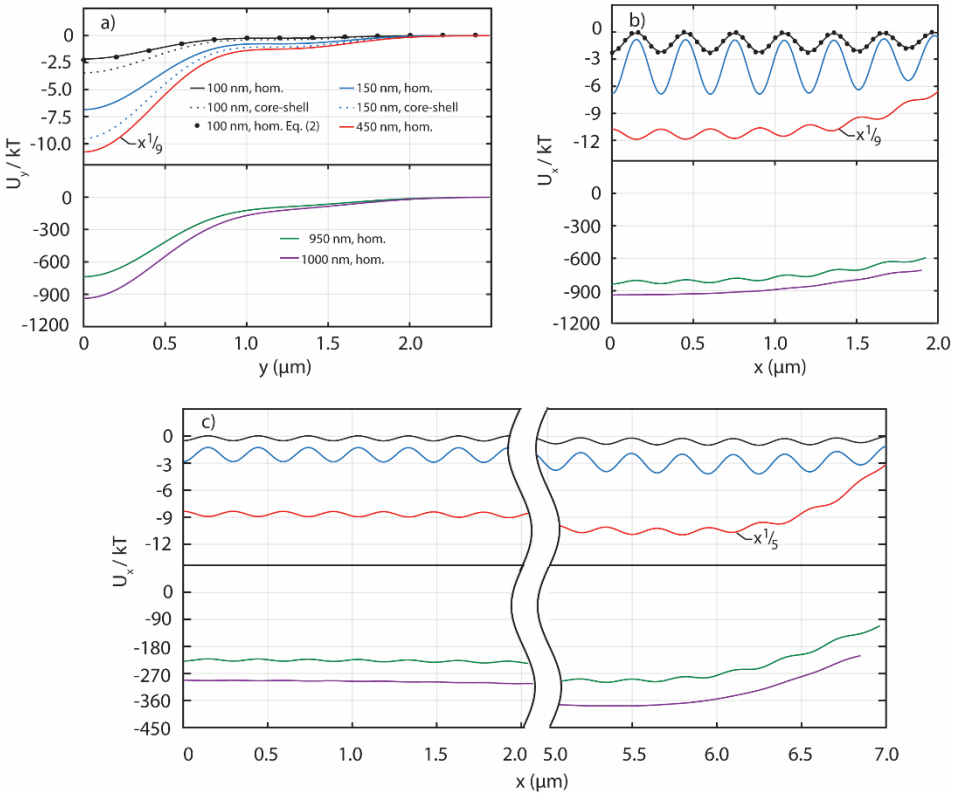

Fig. 5. Normalized trapping potentials for the 5 and 15 μm traps for 100 mW of optical power supplied to the traps, calculated from the force curves in Fig. 4. The legends in (a) define EV sizes and the EV index model (homogeneous versus core-shell) and apply to each panel. (a) transverse potential $U_y(y)/kT$ for the 5 μm. (b). Longitudinal potential $U_x(x)/kT$ for the 5 μm trap. (c) Longitudinal potential $U_x(x)/kT$ for the 15 μm trap, with part of the *x*-axis omitted to obtain the same horizontal scale as in (a) and (b).

In the plot of $U_y(y)/kT$ in Fig. 5(a) it is seen that the 5 μm trap cannot stably trap 100 and 150 nm homogeneous EVs in the *y*-direction at 100 mW. The same holds for the 100 nm core-shell EV. The 150 nm core-shell EV, however, is almost stably trapped, implying that above 150 nm core-shell EVs are all stably trapped at this power level. The potentials for homogeneous EVs of d_{EV} = 450, 950 and 1000 nm each indicate stable trapping.

$U_x(x)/kT$ of the 5 and 15 μm traps shows periodic oscillations of a strength and phase depending on EV size, superimposed on a background potential that depends on EV size as well. Background potential with superimposed oscillations are called global potential. For the smaller EVs the individual wells of the periodic potential are not deep enough for stable

Optics EXPRESS

trapping at 100 mW. Thermally activated hopping between wells will occur. For d_{EV} = 450, 950 nm the individual wells are deep enough for stable trapping, while for these diameters the background potential is more apparent. For d_{EV} = 1000 nm the oscillations are virtually absent, in agreement with the force-cancellation in Fig. 4. Considering the smoother global potentials in more detail and using symmetry w.r.t. x = 0, one recognises a single potential well centred at the origin for the 5 μm trap and a double-well potential for the 15 μm trap (from the potential levels at either side of the cut in Fig. 5(c), one easily sees that the single-sided curves indeed define a double-well potential). These different potential shapes agree with the respective global hot regions for the three traps.

In calculating the potentials we have applied Eqs. (3) and (4), thus stretching the range where the optical force to a good approximation is found to be conservative (up to d_{EV} = 100 nm, see Section 5) to d_{EV} = 1000 nm. To estimate the error we make in this, we have calculated for d_{EV} = 1000 nm and the 5 and 15 μm traps the line integral of the optical force along different escape paths from the trap, starting at the origin. The maximum difference we find for the paths amounts to 10%. We believe this is acceptable, also since this is a worst case scenario: with decreasing EV size the relative contribution of the scattering force becomes smaller, *i.e.* the approximation of conservativity becomes better.

7. Trapping stability

In line with Ashkin's criterion, the minimum power P_{min} for stable trapping of an EV is defined by the demand that the depth of the normalized potential well in the three directions equals 10. We first make this demand explicit for the three potential wells obtained.

The transverse potential well is the well U_y / kT defined by curves as in Fig. 5(a). We take the transverse axis through the x-position of the most intense hot spot, which for the 5, 10 and 15 μm traps is at x = 0, ± 3.6 and ± 6.3 μm, respectively. In Fig. 6(a) U_y / kT is plotted for stable trapping in the 5 μm trap. We define the maximum excursion during confined Brownian motion as the distance from y = 0 to either of the knee points of the curve (indicated by arrows in Fig. 6(a)), which is located closer to y = 0 than the classical turning points at U_y / kT = 10. So, we avoid the strong influence of the very flat wings of the well. We thus get a single-sided excursion of 1.0 μm. The overall picture for U_z / kT is similar.

The deepest local well of the longitudinal potential is, depending on EV size, the deepest local well of U_x / kT at the most intense hot spot or in between the two most intense hot spots (see Fig. 5(b) for these situations). In Fig. 6(b) U_x / kT is plotted for stable trapping in the central local well of the 5 μm trap. Local well depths near the centre being close, this case also represents stable trapping near the center. The single-sided maximum excursion is about 150 nm (i.e., half of the modulation period). Each of the local trapping wells near the center can be filled with one or more EVs. Access to each of these traps can be provided by translating the chip under the microscope objective for Raman spectroscopy or by shifting the interference pattern by applying a phase difference to the beams forming the trap using on-chip heaters.

The global longitudinal potential well U_x / kT is defined as the background potential with superimposed oscillations. EV trapping in the global potential is only fundamentally different from trapping in an individual well if the potential's oscillatory part is weak compared to the background. If not, the EV can still spend considerable time in a single local well or EV motion is dominated by hopping between such wells. With some arbitrariness, we translate this to the additional demand that the ratio of the deepest local well to the global well depth of 10 is smaller than 0.6.

Optics EXPRESS

For the 5 µm trap we find $P_{\min}$ by making the well depth equal to 10 for classical turning points at $x = \pm 1.9$ µm, where the largest EV does just not touch the facet. This also defines the maximum excursion of 1.9 µm. The demand of a weak enough oscillatory potential leads to the condition $d_{\mathrm{EV}} \geq 300$ nm. In Fig. 6(c) U_x / kT is plotted for stable trapping in the global well of the 5 µm trap.

For the 10 and 15 µm traps $P_{\min}$ is chosen such that the barrier height between the global wells of the double-well potential amounts to 10. For these traps the minima of the individual wells coincide with aforementioned positions of the most intense hot spots. Taking half of the maximum double-sided excursion for these asymmetric wells, we get the maximum single-sided excursions 1.8 (3.1) µm for the 10 (15) µm trap. The demand of a weak enough oscillatory potential leads to the condition $d_{\mathrm{EV}} \geq 300$ (400) nm for the 5 (10 and 15) µm trap, while for the 10 µm traps the range 500–650 nm is excluded.

Applying the demand of stable trapping to the three wells leads to the stability curves in Figs. 6(d)-6(f) for the traps. A stability curve is a plot of $P_{\min}$ versus d_{EV}. Points on and above a stability curve define stable trapping, while for points below a curve an EV cannot be stably trapped. Figures 6(d) and 6(e) are for both index models. Figure 6(f) is for the homogeneous index.

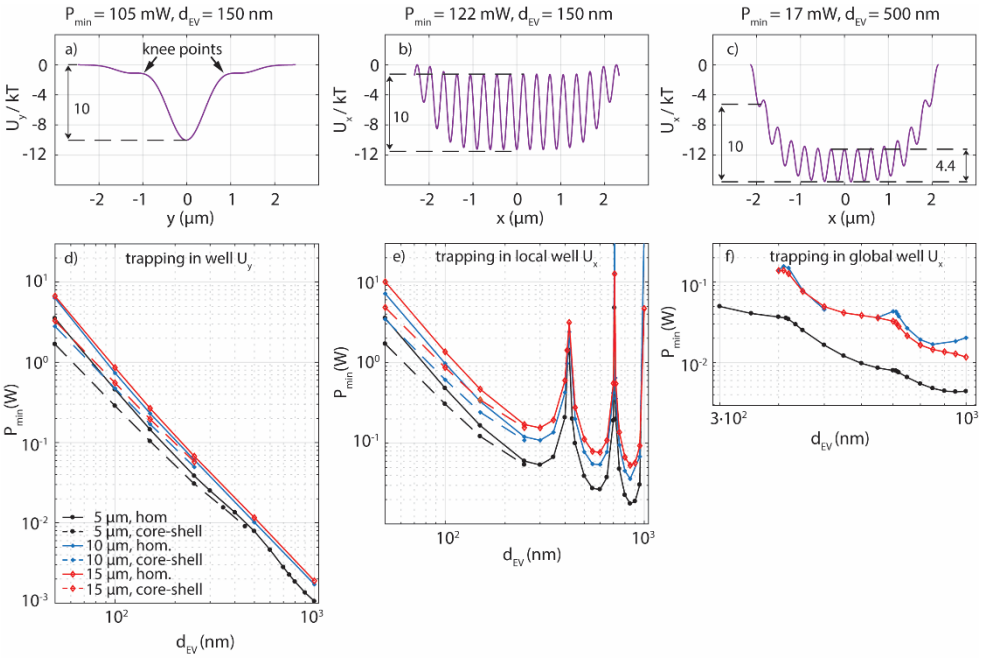

Fig. 6. (a)-(c) Potential wells for the 5 µm trap in case of stable trapping under conditions as indicated above the panels. (a) The transverse well U_y / kT. The indicated knee points limit the confined Brownian motion, as discussed in the text. (b) The deepest local well of U_x / kT. (c) The global well U_x / kT. (d)-(f) Stability curves for the three wells as mentioned in the panels. The legends in (d) define the trap sizes and the EV index model (homogeneous versus core-shell) and apply to each of the stability curves in (d), (e) and (f).

Figure 6(d) for U_y / kT shows that $P_{\min}$ at fixed d_{EV} increases with increasing trap size, the curves for the 10 and 15 µm traps being close. This agrees with the decreasing energy density of the most intense hot spot with increasing trap size in Fig. 3. For small homogeneous

Optics EXPRESS

EVs with $d_{EV} \leq 150$ nm the curves are straight lines of a slope very close to −3. Thus, we approximately have $P_{min} \propto 1/d_{EV}^3$, in agreement with Eq. (2) and therefore with a dominating gradient force. For core-shell EVs with $d_{EV} < 150$ nm, we find $P_{min} \propto d_{EV}^{-2.56}$, while for each trap the core-shell curve lies below the curve for the homogeneous EVs. These properties of the core-shell curves agree with the stronger force acting on core-shell EVs than on homogeneous EVs. Beyond this range, the curves of core-shell EVs asymptotically approach those of homogenous EVs. For 450 nm the effect of the core can still be seen in Fig. 6(d).

In Fig. 6(e), for small d_{EV}, the curves for the deepest local well of U_x / kT show similar behavior as in Fig. 6(d). Different from Fig. 6(d), however, and very prominent are the strong and broad peaks at $d_{EV} \approx 420$, 700 and 1000 nm. For these diameters the oscillatory potential's amplitude is close to zero due to the cancellation effect. As a result, high powers are needed to create deep enough wells for stable trapping.

In Fig. 6(f) the main features are the residues of the peaks in Fig. 6(e). The weakness of these features results from the dominance of the background potential in its interplay with the oscillatory potential. Further comparison of Fig. 6(f) with Fig. 6(e) shows that for each trap the $P_{min} - d_{EV}$ curve for trapping in the global well lies below the curve for trapping in the local well. Thus, when increasing the power at fixed d_{EV}, trapping is first is realized in a global well, followed by trapping in a local well when the power hits the stability curve for local trapping. Finally, by considering the various global potential wells in detail, it is seen that for the 5 µm trap the effect of the oscillations is smallest, as their amplitude is negligible at the classical turning points. For the 10 and 15 µm traps the features are stronger due to relatively strong oscillations present at the barrier of the double-well potential. The curve of the 5 µm trap is below those of the other traps. This relates to energy densities in Fig. (3).

In Figs. 6(d)-6(f) P_{min} covers the range from 1 mW at 1000 nm to 10 W at 50 nm (neglecting the peak values around 700 and 1000 nm). For Raman spectroscopy limited EV excursions in the trap are prefered, suggesting trapping in a local well of U_x / kT. 300 mW can be supported by the glued butt coupling of a fiber to the waveguide facet at the chip edge and by the waveguide itself [32]. The maximum coupling efficiency between fiber and waveguide is 89% [32] and the estimated loss of the Y-junction used [9] to split the entrance waveguide into two waveguides routed to the trapping region is −1.0 dB [32]. We thus arrive at a power of 210 mW available for trapping, which is in the range for Raman spectroscopy on single EVs [10,12]. Figures 6(d) and 6(e) indicate that with the 5 µm trap core-shell EVs of many diameters outside the peaks, down to the smallest diameter of 115 nm, can be trapped for $P_{min} = 210$ mW. In 10 and 15 µm traps this P_{min} enables stable trapping of a core-shell EV as small as 155 and 180 nm, respectively. With these smallest EVs that can be trapped, the largest part of the EV size range is covered. We thus argue that the size range that is adressed with our integrated photonics lab-on-a-chip device is clinically relevant, also in view of the results in [33], where it is demonstrated that already big EVs of a diameter of 1 µm can be used to diagnose prostate cancer.

8. Conclusion and outlook

We have presented the capabilities of dual-waveguide traps based on box-shaped composite SiO_2-Si_3N_4 waveguides for optical trapping of extracellular vesicles (EVs), using FDTD simulations and optical force calculations. EVs are very tiny spherical, cell-derived particles of diameter in the range 30-1000 nm and have a low index contrast w.r.t. water and therefore are hard to trap. EVs attract strong attention as potential markers for cancer.

Owing to both the small size and special structure of the waveguides, the counter-propagating beams are narrow and weakly divergent, properties favorable for a tight optical

Optics EXPRESS

trap. For facet spacings of 5, 10 and 15 μm the optical field between the facets shows clear interference maxima or hot spots, leading to an oscillatory force acting on an EV as a function of its position and thus to multiple trapping sites. For certain EV sizes the forces exerted by several hot spots cancel and only a global longitudinal force remains.

By calculating forces using Lumerical's volumetric technique for EV diameters in the range 50–1000 nm using two refractive index distributions, *viz.* homogeneous and that of the realistic core-shell structure, we find that the shell, though only 5 nm thick, contributes considerably to the force up to a diameter of 450 nm. By comparing these forces with forces obtained using the gradient formula, we conclude that the gradient force clearly dominates the total force up to 100 nm EV diameter. This results from counter-propagation of the beams. Longitudinal trap stiffnesses derived from the force curves are up to ten times higher than the lateral stiffness of a laser-beam trap, a quality resulting from the interference.

The trapping potentials derived from the force curves lead to the so-called stability curves (i.e., curves of the minimum optical power required for stable EV trapping as a function of EV size). These curves indicate that EVs of a wide diameter range can be stably trapped with the attainable trapping power of 210 mW, down to a smallest size of 115 nm for the 5 μm trap. This capability in combination with the power level sufficient for Raman spectroscopy of the trapped EV, qualify this dual-waveguide trap as a promising lab-on-a-chip device with clinical relevance. Finally, we note that the drag force acting on an EV in a trap under fluidic flow can be incorporated in our procedure, leading to modified stability curves. Based on these, the smallest EV that can be stably trapped in the flow situation can again be chosen by setting the optical power, allowing all smaller EVs to be collected downstream. This defines the principle of a size filter for EVs and can be generalized to other bio-particles, such as proteins, cell fragments, and so forth.

As a short outlook, we mention that a multiple-waveguide geometry is a logical extension of the geometry presented here. Multiple waveguides lead to stronger light concentration and thus a stronger trap, since an interference pattern is created with beams coming from many directions. We have a fabrication run underway for dual-, quad-, and octo-waveguide traps tailored for experimental trapping and Raman studies of EVs.

Funding

Netherlands Organisation for Scientific Research (NWO) (14197); NWO Physical Sciences, (15316).

Acknowledgments

The authors thank M.R. Fanood and R.J. Moerland for stimulating discussions, A. Nanou for critical reading of the manuscript and R. Nieuwland for making us aware of reference 14. F. Schreuder, M. Hoekman and A. Leinse are acknowledged for their input on the composite SiO_2-Si_3N_4 (TripleX) waveguides and E. van der Pol and A.G.J.M. van Leeuwen for sharing knowledge on extracellular vesicles. NWO Physical Sciences made the Supercomputer Cartesius available for the simulations (15316).